APPLIED MATHEMATICS AND MECHANICS (ENGLISH EDITION)

Theoretical and experimental study of a bi-stable piezoelectric energy harvester under hybrid galloping and band-limited random excitations[*]

Haitao LI[1], Tianyu ZHENG[1], Weiyang QIN[2], Ruilan TIAN[3],

Hu DING[4,†], J. C. JI[5], Liqun CHEN[4]

1. Department of Engineering Mechanics, North University of China, Taiyuan 030051, China;

2. Department of Engineering Mechanics, Northwestern Polytechnical University, Xi'an 710072, China;

3. Department of Engineering Mechanics, Shijiazhuang Tiedao University, Shijiazhuang 050043, China;

4. Shanghai Key Laboratory of Mechanics in Energy Engineering, Shanghai Frontier Science Center of Mechnoinformatics, Shanghai Institute of Applied Mathematics and Mechanics, School of Mechanics and Engineering Science, Shanghai University, Shanghai 200072, China;

5. School of Mechanical and Mechatronic Engineering, University of Technology Sydney, New South Wales 2007, Australia

(Received Nov. 14, 2023 / Revised Jan. 26, 2024)

Abstract In the practical environment, it is very common for the simultaneous occurrence of base excitation and crosswind. Scavenging the combined energy of vibration and wind with a single energy harvesting structure is fascinating. For this purpose, the effects of the wind speed and random excitation level are investigated with the stochastic averaging method (SAM) based on the energy envelope. The results of the analytical prediction are verified with the Monte-Carlo method (MCM). The numerical simulation shows that the introduction of wind can reduce the critical excitation level for triggering an inter-well jump and make a bi-stable energy harvester (BEH) realize the performance enhancement for a weak base excitation. However, as the strength of the wind increases to a particular level, the influence of the random base excitation on the dynamic responses is weakened, and the system exhibits a periodic galloping response. A comparison between a BEH and a linear energy harvester (LEH) indicates that the BEH demonstrates inferior

performance for high-speed wind. Relevant experiments are conducted to investigate the validity of the theoretical prediction and numerical simulation. The experimental findings also show that strong random excitation is favorable for the BEH in the range of low wind speeds. However, as the speed of the incoming wind is up to a particular level, the disadvantage of the BEH becomes clear and evident.

1   Introduction

Currently, the most common solution for powering wireless sensors relies on electrochemical batteries. Nevertheless, some derivative problems, such as the expensive costs of manual maintenance and unavoidable environmental pollution of water and soil, will result from the extensive use of batteries. Vibration, as a source of renewable energy, is abundant in nature. Vibration energy harvesting, a conversion procedure from low-quality and high-entropy vibration energy to the electricity, has attracted attention around the world[1–3]. A host of previous research works focused on the scheme of linear resonance. However, there will be energy harvesting performance suppression as the condition of resonance is not guaranteed[4–6]. As is generally accepted, most environmental vibration is characterized by low-intensity and wide-bandwidth. For this reason, it is very important to increase the adaptability of harvesters to the excitation of the broadband environment.

With the aim of achieving a broad bandwidth, the frequency tuning methods (including active and passive techniques) were proposed[7–11], and multimodal structures were designed[12]. Recently, the burgeoning development of nonlinearity has been a promising solution to achieving better energy harvesting performance. Enormous nonlinearities including hardening[13–16], softening[17], and impact[18] have been employed for optimizing the energy harvesting performance. Because of the broadband energy harvesting property and excellent output performance when inter-well vibration takes place, the bi-stable energy harvesters (BEHs) have attracted extensive interest[19–26]. Based on the magnetic repulsion and attraction, Stanton et al.[27] and Erturk et al.[28] developed two kinds of bi-stable structures for capturing vibration energy, and they systematically investigated the nonlinear dynamic behaviors such as bifurcation and chaos. Utilizing two external rotational magnets, Cao et al.[29] conducted a comprehensive investigation on the BEH, and found that the proposed structure was preferable to the linear and mono-stable counterparts when it was subject to a deterministic excitation.

Since the vibration energy harvesting efficiency is easily influenced by ambient sources, a number of scholars have devoted themselves to investigating the energy harvesting performance or dynamic behaviors under non-periodic excitations[30–36]. In practice, randomness is the intrinsic characteristic of ambient vibration, and it is usually considered as a broad-band random process. Cottone et al.[32] studied the dynamic response of a pre-load piezoelectric beam under a random excitation. The system generates relatively large electrical energy when the axial preload of the elastic beam is greater than the critical one for realizing buckling. Zhao and Erturk[33] studied the relative superiority of mono-stable and bi-stable energy harvesting structures. The latter could capture more energy if and only if the input excitation exceeds the critical energy for triggering inter-well vibration. To transform the impulsive excitation into a plucking force, Fang et al.[34] designed a kind of BEH with a rotating mechanism and plectrums to achieve high-energy output. Xu et al.[35] found the fluctuation of wind speeds and qualitatively evaluated the galloping-based energy harvesting performance with the stochastic averaging method (SAM). Jiang et al.[36] employed the numerical path integration method to investigate the transient response and obtain a probability density function (PDF) from the transition Fokker-Planck-

Kormogorov (FPK) equation.

In the real world, a great deal of kinetic energy is produced by the movement of air and water current. Converting the inexhaustible energy into electric energy would reduce carbon emission. Among the fluid-structure interaction mechanism, the response amplitude of galloping increases dramatically as the incoming wind speed exceeds the critical cut-in one, and thus it has an advantage in the operational wind speed range[37–43]. Dai et al.[44–45] established a theoretical model of a nonlinear energy harvester based on the Euler-Lagrange method, and investigated the influence of electromagnetic coupling analytically. To enhance the performance of wind-driven energy harvesters at low-speed wind, Zhou et al.[46] optimized the geometry of bluff body and proposed a Y-shaped ornament to adhere on the main structure of the BEH.

To increase the efficiency of energy conversion, scholars devoted themselves to harvesting the base vibration energy and galloping simultaneously[47–49]. Most energy harvesters subject to hybrid base vibration and galloping usually employ linear stiffness, and up to now, there have been only a few studies on the interaction of galloping and base excitation[50–51]. Zhao and Yang[52] proposed an aeroelastic energy harvester with impact nonlinearity, and verified an extended bandwidth for scavenging concurrent wind and vibration. Li et al.[53] investigated the nonlinear dynamic behaviors such as coexisting solutions and harvesting properties of a bi-stable structure under combined harmonic excitation and galloping. Yang et al.[54] studied the steady-state stochastic dynamic response of a linear energy harvester (LEH) under hybrid Gaussian white noise and galloping with the SAM. In the natural environment, airflow has a direct effect on the vibration energy performance, but the combined effect of galloping and random excitation on the BEH is not clear. Therefore, investigating how galloping-random excitation affects the BEH would reveal the synergistic mechanism and realize a performance enhancement.

With the aim to explore the intrinsic correlation between the interaction of two excitations and energy harvesting performance, this paper conducts a theoretical and experimental investigation on the BEH subject to hybrid galloping-random excitations (BEH-GR). The other parts of this work are organized as follows. In Section 2, an explicit expression of the steady-state PDF is obtained by the SAM based on the energy envelope. In Section 3, the analytical results are verified with the numerical simulation based on the Monte-Carlo method (MCM), and an objective comparison between the LEH and the BEH under combined band-limited random excitation and galloping is made. In Section 4, with the simultaneous action of the wind tunnel and shaker, the experimental validation is conducted under combined excitations to verify the numerical comparison between the LEH and the BEH. The conclusions are finally drawn in Section 5.

2   Design and stochastic averaging analysis

Figure 1 shows a structural design diagram of the BEH and describes its operating condition. The proposed energy harvesting structure comprises the following parts: a steel cantilever elastic beam, a piezoelectric sheet, and a half cylinder. A piezoelectric sheet is stuck to the adjacent region of the fixed end. The geometric dimensions of the beam and piezoelectric layer can be demonstrated as $L_b \times w_b \times h_b$ and $L_p \times w_p \times h_p$, respectively. In the above representation, L, w, and h with the subscripts b and p denote the length, width, and thickness of the beam and piezoelectric layer, respectively. The direct piezoelectric effect can be characterized by the parameters of the electro-mechanical coupling e_{31} and permittivity e_{33}. Three permanent NdFeB magnets are included in the design, where one magnet is attached on the lower edge of the free end of the elastic beam, while the other two stationary magnets are attached on the T-shaped holder. Especially, the energy harvester is simultaneously influenced by the base excitation $y(t)$ and the aerodynamic load. With the Euler-Lagrange method and single mode assumption, the governing equations can be represented as follows[53]:
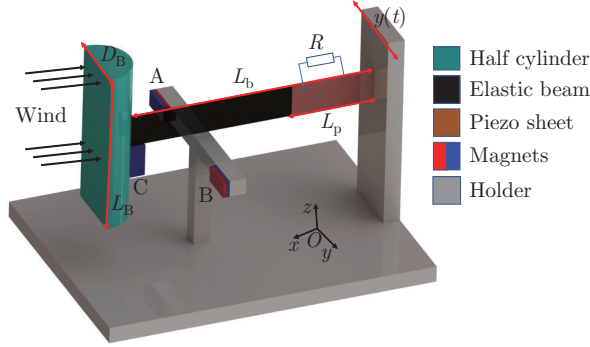
Fig. 1 The structural design of the BEH-GR, which is simultaneously influenced by galloping and random excitation (color online)

$$\begin{cases} M\ddot{q} + 2M\xi\omega_1\dot{q} + (K + K_1)q + K_2q^3 + K_3q^5 - \Theta V \\ = -N\ddot{y} + \dfrac{1}{2}\rho_a D_B L_B U^2 \displaystyle\sum_{i=1}^{3} a_i\Big(\dfrac{\dot{q}+\dot{y}}{U}\Big)^i, \\ \dfrac{1}{2}C_p\dot{V} + \dfrac{V}{R} + \Theta\dot{q} = 0, \end{cases} \quad (1)$$

where M and K represent the distributed expressions of mass and stiffness, respectively. w_1 and ξ means the first order resonant frequency and the damping ratio, respectively. K_i $(i = 1, 2, 3)$ represent the coefficients of nonlinear magnetic force. Θ represents the equivalent electromechanical coupling factor. N indicates the coefficient of external base excitation. ρ_a represents the air density at normal temperature, L_B and D_B denote the height and cross-flow width of the bluff body, respectively. U is the velocity of the incoming flow, and a_i $(i = 1, 2, 3)$ represent the empirical coefficients of the aerodynamic load, which are determined by the least squares method. C_p indicates the electric capacity of the piezoelectric sheet. V denotes the generated voltage in pure resistance circuit.

To conduct the stochastic averaging analysis, the dimensions of Eq. (1) are removed by introducing the following dimensionless parameters:

$$\bar{q} = \frac{q}{L_b}, \quad t = \omega_1\tau, \quad \omega_1 = \sqrt{(K + K_1)/M}, \quad v = \frac{\theta L_b}{C_p}V,$$

$$\alpha_1 = \frac{K_2 L_b{}^2}{K + K_1}, \quad \alpha_2 = \frac{K_3 L_b{}^4}{K + K_1}, \quad \kappa = \frac{\theta^2}{C_p(K + K_1)}, \quad f = \frac{N}{ML_b},$$

$$\overline{U} = \frac{U}{\omega_1 L_b}, \quad \mu = \frac{\rho_a D_B L_B L_b}{M}, \quad \lambda = \frac{2}{R\omega_1 C_p}, \quad \xi = \frac{c}{2M\omega_1}.$$

Using the above transformation, one can obtain the following dimensionless equations:

$$\begin{cases} \ddot{\bar{q}} + (2\xi - \mu a_1\overline{U})\dot{\bar{q}} + \bar{q} + \alpha_1\bar{q}^3 + \alpha_2\bar{q}^5 + \dfrac{\mu a_3}{\overline{U}}\dot{\bar{q}}^3 - \kappa v = -f\ddot{y}, \\ \dot{v} + \lambda v + \dot{\bar{q}} = 0, \end{cases} \quad (2)$$

where α_1 and α_2 are the dimensionless nonlinear stiffnesses. $\overline{U}$ refers to the dimensionless speed of the incoming wind, and represents the electromechanical coupling constant. μ is a proportionality factor of the inertia of flow and mass, λ is the dimensionless time factor, and f is the coefficient of external base acceleration.

In this paper, the base acceleration excitation $\ddot{y}(t)$ is described as a Gaussian white noise process with a particular bandwidth. The correlation function can be represented as

$$G(\omega) = \begin{cases} 2D\delta(\tau), & \omega_{\mathrm{c}} - \dfrac{B}{2} \leqslant \omega \leqslant \omega_{\mathrm{c}} + \dfrac{B}{2}, \\ 0, & \text{else,} \end{cases} \tag{3}$$

in which $\delta(\cdot)$ means the Dirac function, and $2D$ represents the level of the band-limited Gaussian random excitation. ω_{c} and B are the central frequency and bandwidth of the power density, respectively.

Integrate the electrical equation in Eq. (3), and express the analytical function of voltage as

$$v(t) = B_1 \mathrm{e}^{-\lambda \mathrm{t}} + \int_0^t \mathrm{e}^{-\lambda(t-\tau)} \dot{\overline{q}}(t-\tau)\mathrm{d}\tau, \tag{4}$$

where B_1 is a constant estimated by the voltage at the initial stage. $B_1 \mathrm{e}^{-\lambda t}$ has no remarkable influence along with the decay of the exponent. Hence, the voltage is rewritten as

$$v(t) = \int_0^t \dot{\overline{q}}(\tau)\mathrm{e}^{-\lambda(t-\tau)}\mathrm{d}\tau. \tag{5}$$

According to the generalized harmonic transformation, the equivalent displacement and velocity in the system (2) are written as

$$\begin{cases} \overline{q} = A(H)\cos(\omega(H)t) \pm \overline{q}^*, \\ \dot{\overline{q}} = -A(H)\omega(H)\sin(\omega(H)t), \end{cases} \tag{6}$$

where H represents the mechanical energy of the conservative system. $A(H)$ and $\omega(H)$ mean the amplitude response and frequency, respectively, which are the functions of energy. $\overline{q}^*$ is the equilibrium, and the system realizes snap-through for $\overline{q}^* = 0$.

Based on Eqs. (6) and (7), the voltage is explicitly expressed as

$$v(t) = \begin{cases} \dfrac{\omega^2(H)}{\lambda^2 + \omega^2(H)}(\overline{q} \pm \overline{q}^*) + \dfrac{\lambda^2}{\lambda^2 + \omega^2(H)}\dot{\overline{q}}, & \text{intra-well}, \\ \dfrac{\omega^2(H)}{\lambda^2 + \omega^2(H)}\overline{q} + \dfrac{\lambda^2}{\lambda^2 + \omega^2(H)}\dot{\overline{q}}, & \text{inter-well}. \end{cases} \tag{7}$$

For a given energy H, the dimensionless frequency is expressed as $\omega(H) = \dfrac{2\pi}{T(H)}$, where $T(H)$ is the vibration period of the conservative system. On the basis of the motion characteristics of the undamped oscillator, it is well known that the period can also be described as $T(H) = \oint \dfrac{\mathrm{d}x}{\sqrt{2H - 2\Pi(x)}}$, where Π is the equivalent potential energy of the non-dimensional system.

Substituting Eq. (7) into the second equation of Eq. (2) gives the equivalent dynamic equation as

$$\ddot{\overline{q}} + \left(2\xi - \mu a_1 \overline{U} - \frac{\lambda^2 \kappa}{\lambda^2 + \omega^2(H)}\right)\dot{\overline{q}} + \overline{q} + \alpha_1 \overline{q}^3 + \alpha_2 \overline{q}^5 + \frac{\mu a_3}{\overline{U}}\dot{\overline{q}}^3$$

$$- \frac{\kappa \omega^2(H)}{\lambda^2 + \omega^2(H)}(\overline{q} + (-1)^{i+1}\overline{q}^*) = -f\ddot{y}, \quad i = 1, 2, 3, \tag{8}$$

where $i = 1, 2$ mean the intra-well responses, while $i = 3$ corresponds to the inter-well response, and $\overline{q}^* = 0$.

With the first integral, the mechanical energy of the corresponding dynamic system (8) is derived as

$$H = \frac{1}{2}\dot{\overline{q}}^2 + \frac{1}{2}\overline{q}^2 + \frac{\alpha_1}{4}\overline{q}^4 + \frac{\alpha_2}{6}\overline{q}^6 - \frac{1}{2}\frac{\kappa\omega^2}{\lambda^2 + \omega^2}\overline{q}^2. \tag{9}$$

The modified system can be rewritten as two first-order ordinary differential equations,

$$\begin{cases} \dot{\overline{q}} = \pm\sqrt{2H - 2\Pi(\overline{q})}, \\ \dot{H} = -\dot{\overline{q}}f(\overline{q},\dot{\overline{q}}) + \dot{\overline{q}}\xi(t), \end{cases} \tag{10}$$

where $\Pi(\overline{q})$ is the potential energy, and it is expressed as $\Pi(\overline{q}) = -\frac{1}{2}\overline{q}^2 + \frac{\alpha_1}{4}\overline{q}^4 + \frac{\alpha_2}{4}\overline{q}^6 + \frac{1}{2}\frac{\kappa\omega^2}{\lambda^2 + \omega^2}\overline{q}^2$, and $f(\overline{q},\dot{\overline{q}}) = \left(2\xi - \mu a_1\overline{U} + \frac{\lambda^2\kappa}{\lambda^2 + \omega^2}\right)\dot{\overline{q}} - \frac{\mu a_3}{\overline{U}}\dot{\overline{q}}^3 + \frac{\kappa\omega^2}{\lambda^2 + \omega^2}\overline{q}^*$.

Then, the averaged Itô equation can be expressed in terms of the total energy H and the Wiener process $B_w(t)$ in the form of

$$dH = m(H)dt + \sigma(H)dB_w(t), \tag{11}$$

where $m(H)$ and $\sigma(H)$ represent the effects of drift and diffusion, which can be determined by the following equations, respectively:

$$m(H) = -\langle\dot{\overline{q}}f(\overline{q},\dot{\overline{q}})\rangle_t + D = -\frac{1}{T(H)}\oint f(\overline{q},\dot{\overline{q}})d\overline{q} + D = -\frac{2}{T(H)}\int_{A_1}^{A_2} f(\overline{q},\dot{\overline{q}})d\overline{q} + D, \tag{12}$$

$$\sigma(H) = 2D\langle\dot{\overline{q}}^2\rangle_t = \frac{2D}{T(H)}\oint \dot{\overline{q}}d\overline{q} = \frac{4D}{T(H)}\int_{A_1}^{A_2} \sqrt{2H - 2\Pi}d\overline{q}, \tag{13}$$

where $\langle\cdot\rangle_t$ denotes the average over one quasi-period. A_1 and A_2 indicate the maximum and minimum amplitudes, respectively, and can be determined by $H = \Pi(A_i)\,(i = 1, 2)$. The energy-variable frequency is obtained by solving the functional relation of $\omega(H) = 2\pi/T(H)$ with the iterative method.

To obtain the analytical form of stationary probability density, the following reduced FPK equation is solved:

$$\frac{1}{2}\frac{\partial^2(\sigma^2(H)p(H))}{\partial H^2} - \frac{\partial(m(H))}{\partial H} = 0. \tag{14}$$

Then, the analytical PDF with respect to the mechanical energy H can be derived as

$$p(H) = C_0\exp\left(\int_0^H \frac{m(H)}{\sigma^2(H)}du\right)\bigg/\sigma^2(H), \tag{15}$$

where C_0 is a constant for normalization. The joint probability density function (JPDF) about the equivalent mechanical state variable is expressed as

$$p(\overline{q},\dot{\overline{q}}) = \frac{p(H)}{T(H)}\bigg|_{H=H(\overline{q},\dot{\overline{q}})}. \tag{16}$$

The average of the squared electric voltage is expressed by Eq. (7),

$$E(v^2) = \int_{-\infty}^{\infty}\int_{-\infty}^{\infty}\left(\frac{\omega^2(H)}{\lambda^2 + \omega^2(H)}(\overline{q} \pm \overline{q}^*) + \frac{\lambda^2}{\lambda^2 + \omega^2(H)}\dot{\overline{q}}\right)^2 p(\overline{q},\dot{\overline{q}})d\overline{q}d\dot{\overline{q}}. \tag{17}$$

As a result, the expected value of output power $E(P)$ is defined as follows:

$$E(P) = \lambda\kappa E(v^2). \tag{18}$$

3   Numerical simulations and discussion

In the following section, numerical simulations are carried out to prove the theoretical analysis of the SAM, and to compare the stochastic dynamic behaviors of the LEH and BEH under hybrid excitation with the MCM. Table 1 shows the dominant model parameters in simulations and experiments. For the sake of generating a band-limited excitation, the Gaussian white noise is first obtained and then passes through a Butterworth bandpass filter. Typically, the band-limited random excitation is represented by bandwidth, central frequency, and power spectral density (PSD). Integrating the PSD along the bandwidth and making a square root will determine the excitation level.

Table 1   Parameters of the piezo-aeroelastic energy harvester in numerical simulation and experiment

Physic description/notation	Value	Physic description/notation	Value
Elastic beam length L_b	0.15 m	Piezoelectric strain coefficient e_{31}	$-11.6 \, \text{C} \cdot \text{m}^{-2}$
Elastic beam width w_b	0.015 m	Piezoelectric permittivity e_{33}	$3.18 \times 10^{-8} \, \text{nF} \cdot \text{m}^{-1}$
Elastic beam thickness h_b	4×10^{-4} m	Projection distances between magnets a and d	0.022 m, 0.021 m
Elastic beam Young's modulus Y_b	210 GPa	Magnet size V_m	$1.2 \times 10^{-6} \, \text{m}^3$
Elastic beam density ρ_b	$7\,800 \, \text{kg} \cdot \text{m}^{-3}$	Magnetization intensity M_j	$0.8 \times 10^6 \, \text{Am}^{-1}$
Piezoelectric sheet length L_p	0.028 m	Half cylinder diameter D_B	0.032 m
Piezoelectric sheet thickness h_p	3×10^{-4} m	Half cylinder height L_B	0.107 m
Piezoelectric sheet width w_p	0.01 m	Half cylinder mass M_E	0.004 kg
Piezoelectric sheet density ρ_p	$4\,000 \, \text{kg} \cdot \text{m}^{-3}$	Mechanical damping ratio ξ	0.005 1
Piezoelectric sheet Young's modulus C_{11}^E	67 GPa	Aerodynamic coefficients (a_1, a_2, a_3)	$(1.56, 0, -6.9)$

Figure 2(a) shows the total energy with the Hamilton function (9) for the non-dimensional parameters of $\alpha_1 = 0.05$, $\alpha_2 = 0.75$, $\kappa = 0.01$, and $\lambda = 0.05$. The red area is the zero total energy surface. As demonstrated in Fig. 2(b), the frequency of the system (2) is not a constant but a variable related to the total mechanical energy. The non-dimensional energy-dependent frequency ranges from 0.5 to 3 for the given parameters, and it presents two local maximum values at two symmetrical equilibria.
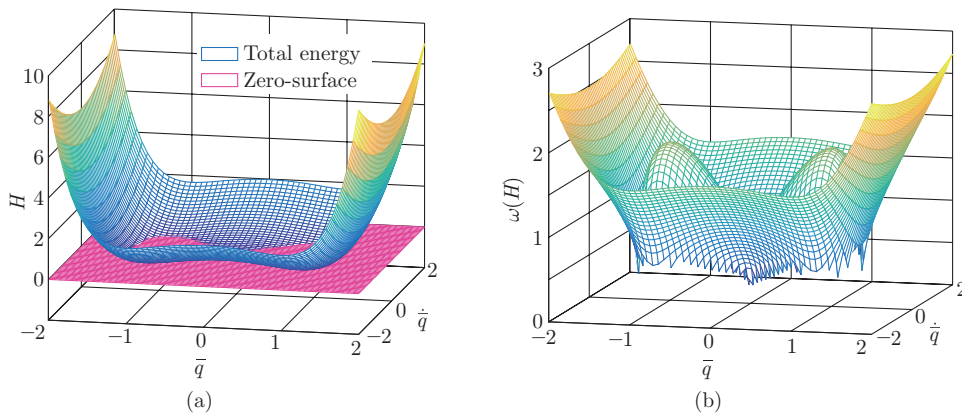

Fig. 2   (a) Total mechanical energy and (b) energy-variable frequency $\omega(H)$ of the unperturbed system (color online)

The stochastic dynamic responses of BEH-GR are comprehensively analyzed by using theoretical calculations with the SAM and numerical simulations with the MCM. Figures 3(a)–3(f)

illustrate the three-dimensional (3-D) JPDF $p(\overline{q}, \dot{\overline{q}})$ for three random excitation levels. The results show that the numerical result is consistent with the analytical result in terms of the 3-D morphology and amplitudes. As the random excitation level is set to $D = 0.2$, it is noted that the marginal probability density function (MPDF) of displacements at the location of $\overline{q} = 0$ tends to zero, which indicates that the dominant response presents the intra-well vibration. As the random excitation level sets to $D = 0.4$, the JPDF around the position of $\overline{q} = 0$ and $\dot{\overline{q}} = 0$ increases gradually, while the one around the equilibrium decreases obviously. The extended area for $p(\overline{q}, \dot{\overline{q}}) > 0$ indicates a higher probability of jumping between potential wells. For all random acceleration levels, a bimodal MPDF of $p(\overline{q})$ is presented in Fig. 3(g). The solid curves demonstrate the analytical results, and the dashed lines are the numerical results of the MCM. The relative error between the prediction of the SAM and verification of the MCM is small, and thus the SAM provides an efficient way for predicting the steady response under band-limited random excitations. Figure 3(h) shows the time histories of displacement and voltage. It is obvious that a large transient voltage will be achieved at the moment of jumping. As a result, frequent jumping between potential wells helps to increase the mean square voltage output.
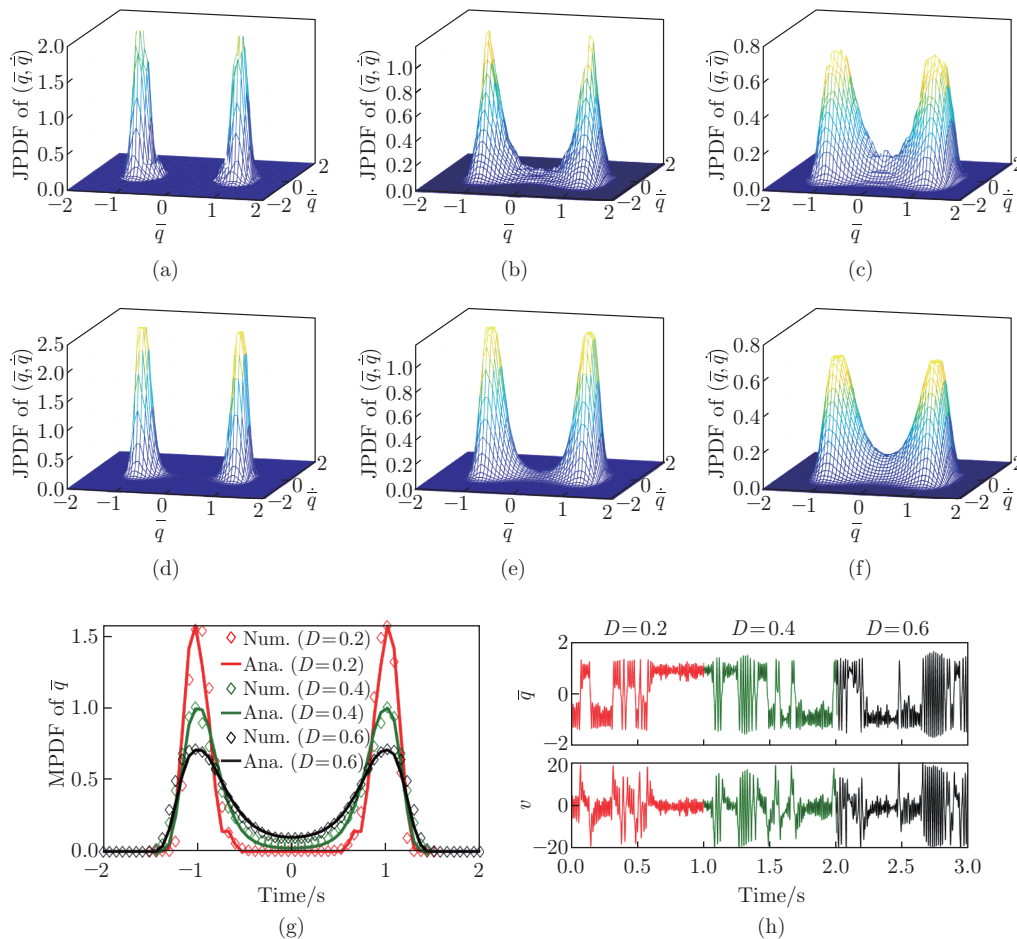

Fig. 3 Comparison of theoretical predictions and numerical simulations for $D = 0.2$, $D = 0.4$, and $D = 0.6$. (a), (b), and (c): 3-D analytical prediction of JPDF with the SAM; (d), (e), and (f): 3-D numerical simulation of JPDF with the Euler-Maruyama method; (g) and (h): MPDF and time domain response for three random excitation levels ("Num." means numerical and "Ana." means analytical) (color online)

Figure 4 indicates the JPDF of BEH-GR for four wind speeds. As the speed of wind reaches 1 m/s and 1.5 m/s, the PDF at two equilibria is significantly higher than at any other positions in the phase plane, indicating that the intra-well response under band-limited random excitation is dominant. As the velocity of incoming wind attains 2 m/s, the response demonstrates the property of periodic galloping, and the 3-D contour diagram of $p\left(\overline{q}, \dot{\overline{q}}\right) > 0$ exhibits an annulus. When the speed of wind increases to 2.5 m/s, a large-amplitude response is observed, and the width of the annulus becomes wider. In summary, an increase in the wind speed will reduce the peak of the probability density at a given location around the equilibrium. In addition, a more evenly distributed PDF indicates the frequent occurrence of the expected inter-well oscillation.
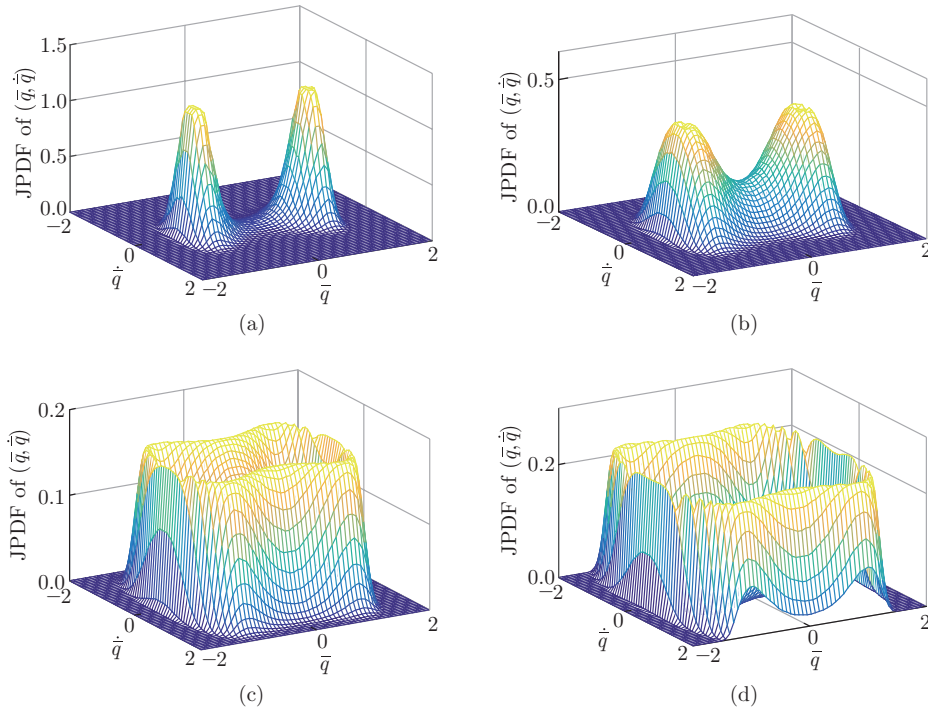

Fig. 4   JPDFs of a BEH-GR for four wind speeds. (a) $\overline{U} = 1$; (b) $\overline{U} = 1.5$; (c) $\overline{U} = 2$; (d) $\overline{U} = 2.5$ (color online)

Figure 5 illustrates the curve of the average power $E(P)$ with respect to the electromechanical coupling factor κ and the time constant λ. The solid lines are the analytical predictions with the SAM, and the dashed lines indicate the numerical results. As the electromechanical coupling factor κ increases, the average output power increases monotonously. But as the time constant λ increases, the average power first increases then decreases, and $E(P)$ realizes the maximum output power at $\lambda \approx 1.3$. Thus, it is indicated that the BEH-GR can achieve an optimum energy conversion performance at the matching impedance.

Figures 6(a) and 6(b) demonstrate 3-D diagrams of acceleration-wind speed-root mean square (RMS) voltage and acceleration-wind speed-standard deviation (SD) displacement, respectively. To ascertain the steady-state dynamic behaviors, the simulation duration is fixed to 200 s. The values of RMS voltage and SD displacement are obtained by taking the statistical analysis and averaging on the data of 20 full-time series of displacements. Based on the relation between the wind speed and response, the diagrams can be divided into three categories. When the simulated speed of wind sets to $U = 1$ m/s, in contrast with the LEH under hybrid galloping and random excitation (LEH-GR), the BEH under random excitation has a significant
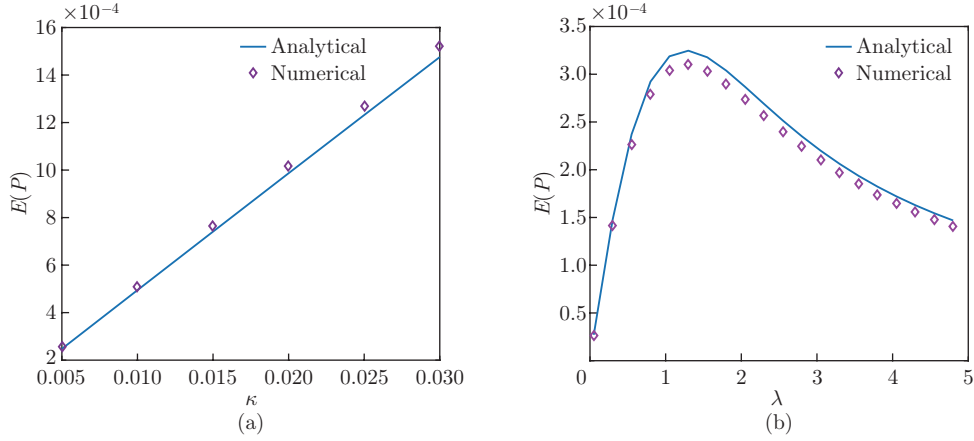
Fig. 5 Curves of the average output power: (a) the effect of electro-mechanical coupling coefficient κ; (b) the effect of time constant ratio λ (color online)
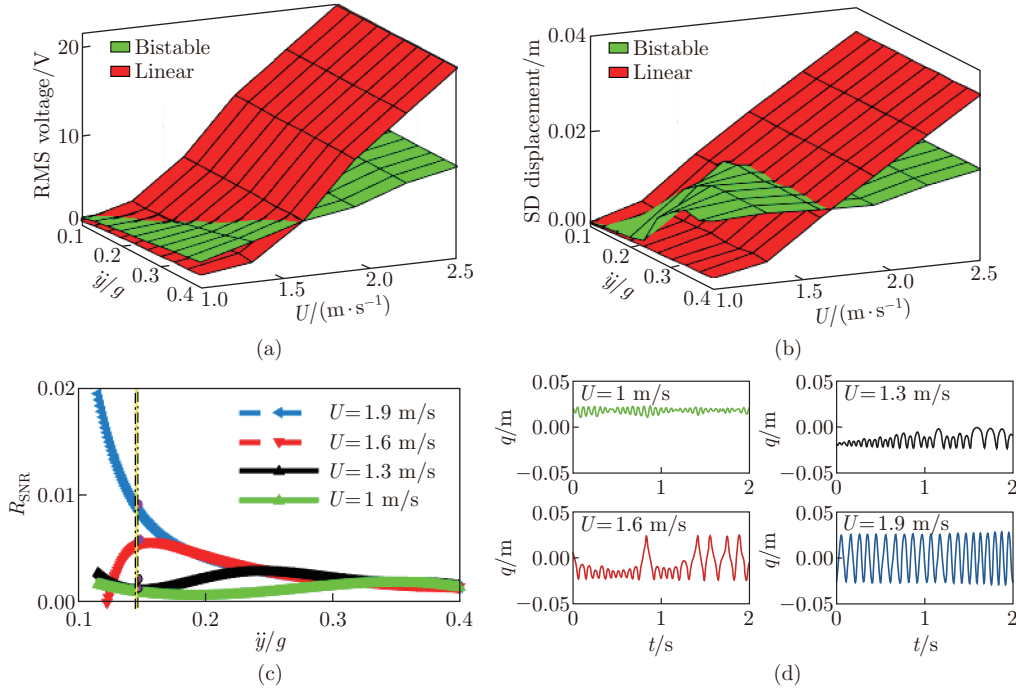

Fig. 6 (a) 3-D diagram of acceleration-wind speed-RMS voltage; (b) 3-D diagram of acceleration-wind speed-SD displacement; (c) R_{SNR} curve; (d) simulated time histories of displacements for $U = 1\,\mathrm{m/s}$, $U = 1.3\,\mathrm{m/s}$, $U = 1.6\,\mathrm{m/s}$, and $U = 1.9\,\mathrm{m/s}$ (color online)

advantage in improving the output response. As the speed of wind increases to the range of $[1.3\,\mathrm{m/s}, 1.6\,\mathrm{m/s}]$, the LEH starts to outperform the BEH at lower excitation levels. If the speed of wind exceeds $U = 1.6\,\mathrm{m/s}$, the LEH presents overwhelmingly superior performance in the responses of displacements and voltages. To show the energy conversion efficiency objectively, an indicator of signal-to-noise ratio (R_{SNR}) is used to measure the ratio between input and output. R_{SNR} is denoted by $R_{\mathrm{SNR}} = \sigma_q/\sigma_{\ddot{y}}$[10], where σ_q and $\sigma_{\ddot{y}}$ mean the SDs of displacement and band-limited random excitation levels, respectively. Figure 6(c) illustrates the parabolic curves of R_{SNR}. The peak of R_{SNR} is associated with the critical excitation level for inducing

stochastic coherence resonance, and the system performs almost regular inter-well response. When the wind speed is $U = 1\,\mathrm{m/s}$, an obvious jump is demonstrated at $\ddot{y} = 0.35g$. Next, as the wind speed increases to $U = 1.3\,\mathrm{m/s}$ and $U = 1.6\,\mathrm{m/s}$, there appear some prominent peaks in the curve of R_{SNR} at $\ddot{y} = 0.25g$ and $\ddot{y} = 0.14g$, respectively. This indicates that the weak wind is conducive to reducing the random excitation level to realize snap-through. When the speed of wind reaches $U = 1.9\,\mathrm{m/s}$, there presents a monotonic property in R_{SNR} because the system generates nearly periodic vibration regardless of the random excitation level. Thus, the increase in the wind kinetic energy weakens the contribution of random base excitation, and increases the generated voltage by triggering the frequent movement among two stable equilibria. Figure 6(d) shows the time histories of BEH for a random excitation level of $0.15g$. It can be seen that the system realizes inter-well response at $U = 1.6\,\mathrm{m/s}$, and the occurrence of jumping between adjacent well is more frequent with the increase in wind speed.

The time histories of the displacement and the corresponding generated voltage of LEH-GR for four wind speeds are demonstrated in Fig. 7. As the speed of wind sets to $U = 1\,\mathrm{m/s}$ and $U = 1.5\,\mathrm{m/s}$, the response increases monotonically with a random excitation level, and the peak-to-peak voltage could attain $12.2\,\mathrm{V}$ and $38.7\,\mathrm{V}$. Finally, as the speed of wind sets to $U = 2\,\mathrm{m/s}$ and $U = 2.5\,\mathrm{m/s}$, the response amplitude is similar for all random excitation levels, and the peak-to-peak voltage could attain $90.9\,\mathrm{V}$ and $109.7\,\mathrm{V}$, respectively.
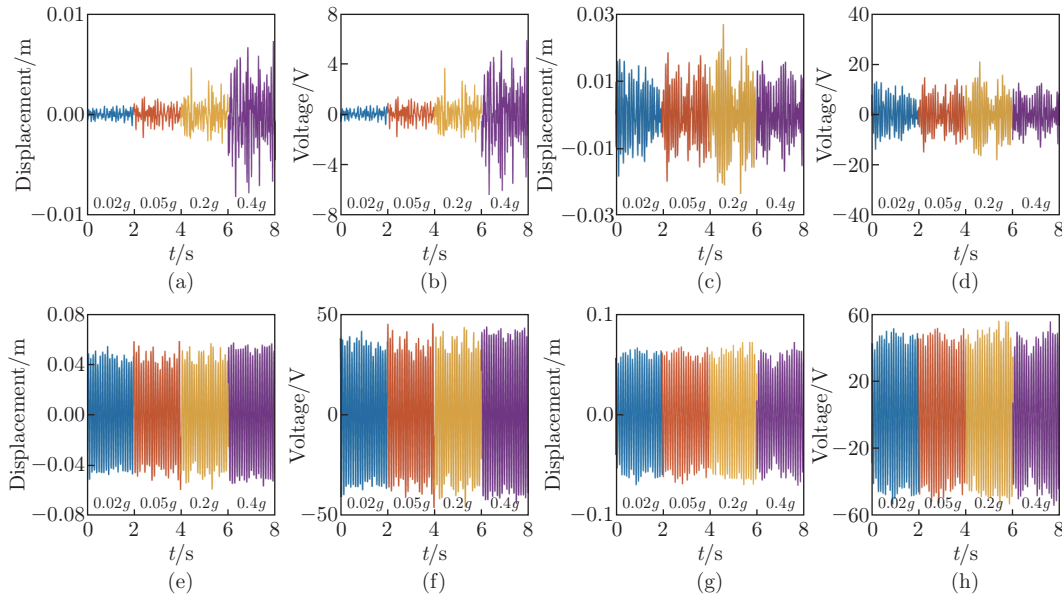

Fig. 7 Simulated time-domain responses of LEH-GR at four wind speeds. (a) and (b): $U = 1\,\mathrm{m/s}$; (c) and (d): $U = 1.5\,\mathrm{m/s}$; (e) and (f): $U = 2\,\mathrm{m/s}$; (g) and (h): $U = 2.5\,\mathrm{m/s}$. The lines of blue, brown, yellow, and purple represent the time domain displacement responses under the random excitation levels of $0.02g$, $0.05g$, $0.2g$, and $0.4g$, respectively (color online)

Figure 8 illustrates the time histories of the displacements and the corresponding generated voltages of the BEH-GR at four specific wind speeds. At two wind speeds of $U = 1\,\mathrm{m/s}$ and $U = 1.5\,\mathrm{m/s}$, inter-well vibration in a bi-stable system cannot occur until excitation increases to $0.4g$ and $0.3g$, and the peak-to-peak values of displacements and voltages could be up to $0.06\,\mathrm{m}$ and $51.0\,\mathrm{V}$ and $0.62\,\mathrm{m}$ and $55.4\,\mathrm{V}$, respectively. As the wind velocity sets to $U = 2\,\mathrm{m/s}$, there is a jump between two potential wells at an excitation level of $0.2g$, and the peak-to-peak values of displacements and voltages could be up to $0.07\,\mathrm{m}$ and $56.0\,\mathrm{V}$, respectively. Finally, as the speed of wind attains $U = 2.5\,\mathrm{m/s}$, double-well vibration around two stable equilibrium

positions are achieved at all four excitation levels. Moreover, although the system is subject to the low-level random excitation, a denser periodic voltage is produced. By comparing the responses at four wind speeds, one can evidently find that the consideration of galloping could trigger inter-well vibration at low-level random excitations. Moreover, with the increase in the simulated wind speed, the response is dominated by galloping gradually, and the stochasticity of the response is gradually reduced.
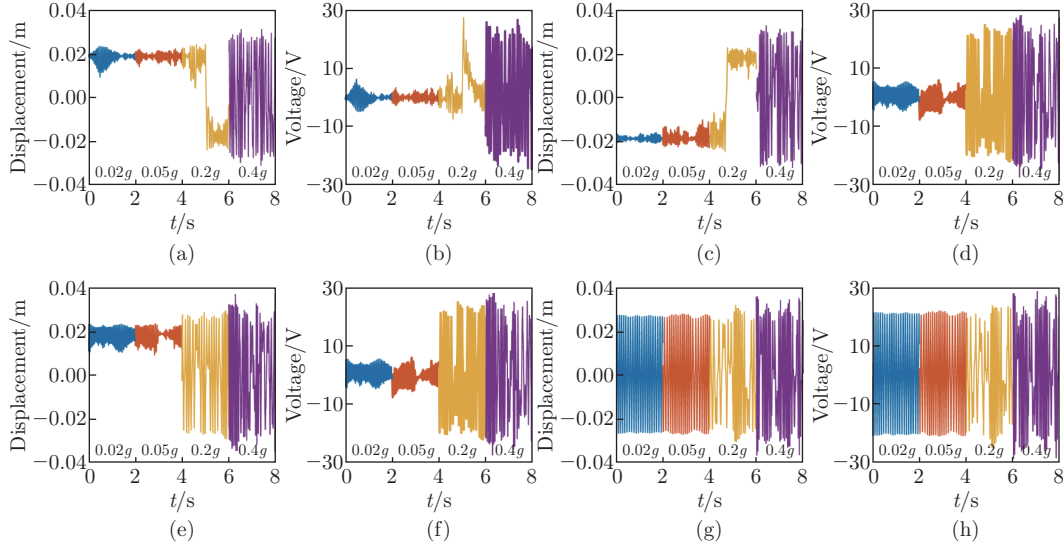

Fig. 8 Simulated time-domain responses of BEH-GR at four wind speeds. (a) and (b): $U = 1\,\text{m/s}$; (c) and (d): $U = 1.5\,\text{m/s}$; (e) and (f): $U = 2\,\text{m/s}$; (g) and (h): $U = 2.5\,\text{m/s}$. The lines of blue, brown, yellow, and purple represent the time domain displacement responses under the random excitation levels of $0.02g$, $0.05g$, $0.2g$, and $0.4g$, respectively (color online)

As seen in Figs. 7 and 8, at low wind speeds, increasing the random excitation levels is helpful to achieving inter-well jumps in the bi-stable system and to producing a prominent voltage output. On the contrary, at high wind speeds, the contribution of the random base excitation is suppressed. Moreover, the amplitude of the BEH is limited by the restoring force, and the response amplitude is lower than that of the linear counterpart.

4 Experimental findings

In this section, experiments are carried out to verify the dynamic response of the numerical simulation. The testing platform is set up as shown in Fig. 9. The fabricated BEH contains a cantilever steel beam, a piezoelectric sheet, and a D-sectional prism ($D_\text{B} \times L_\text{B} = 6\,\text{cm} \times 10\,\text{cm}$). To realize the bi-stable restoring force, one magnet is mounted to the free end of the beam, and the other two fixed permanent magnets are attached on the fixture. In order to achieve long-term stable force-electricity conversion results, a piezoelectric patch micro fiber composite (MFC) M2807P2, Smart Material Corporation) with a better piezoelectric coupling coefficient and flexibility is selected. The energy harvester is mounted on the working table of the electromagnetic shaker (LT-50, Econ Corporation), which provides the transverse random base excitation. A wind tunnel made of an acrylic pipe is used to provide uniform wind. The velocity of the incoming wind is adjusted by a variable frequency drive inverter, and the speed measurement is achieved by a hot wire anemometer (GM8903, Bnetech). A closed-loop vibration level control system consists of a controller (VT-9008, Econ Corporation), accelerometers (14 100, Econ Corporation), and a power amplifier (LA-200, Econ Corporation). A laser sensor

(OptoNCDT1620, Micro-Epsion) and a mixed-domain oscilloscope (MDO3024, Tektronix) are combined to realize non-contact measurement, display and save the dynamic response. A high-impedance probe of the oscilloscope (TPP0205, Tektronix, $10^7\,\Omega$) is used to guarantee that the voltage is measured in an open-circuit condition.
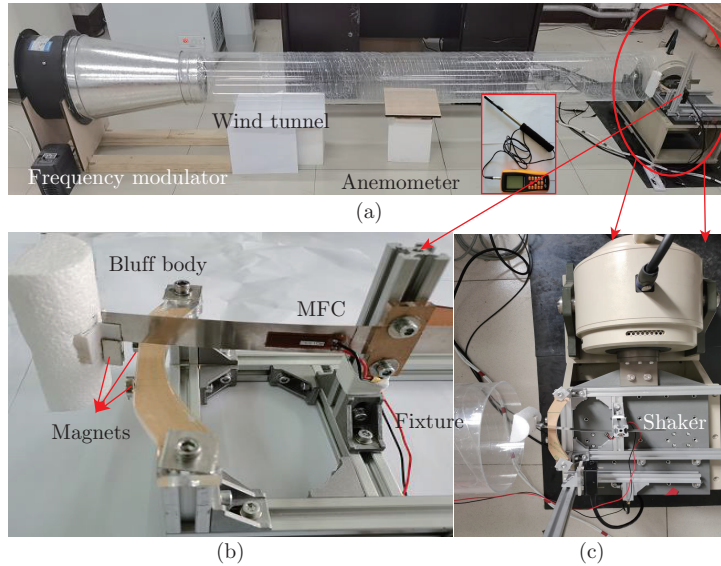

Fig. 9 Experimental setup of BEH-GR: (a) general layout; (b) enlarged view of the BEH; (c) top view of the BEH under hybrid excitation (color online)

To experimentally verify the numerical discussion on the effects of wind and acceleration, Fig. 10 shows a 3-D diagram of the acceleration-wind speed-RMS voltage in an open-circuit condition and the acceleration-wind speed-SD displacement. Four wind speeds (1 m/s, 1.5 m/s, 2 m/s, and 2.5 m/s) and four accelerations (0.02g, 0.05g, 0.2g, and 0.4g) are selected for carrying out an orthogonal experiment. It should be noticed that the increases in the wind speed and random acceleration both result in performance enhancements of mechanical response and electrical response. For low incoming wind speeds and high accelerations, the BEH provides
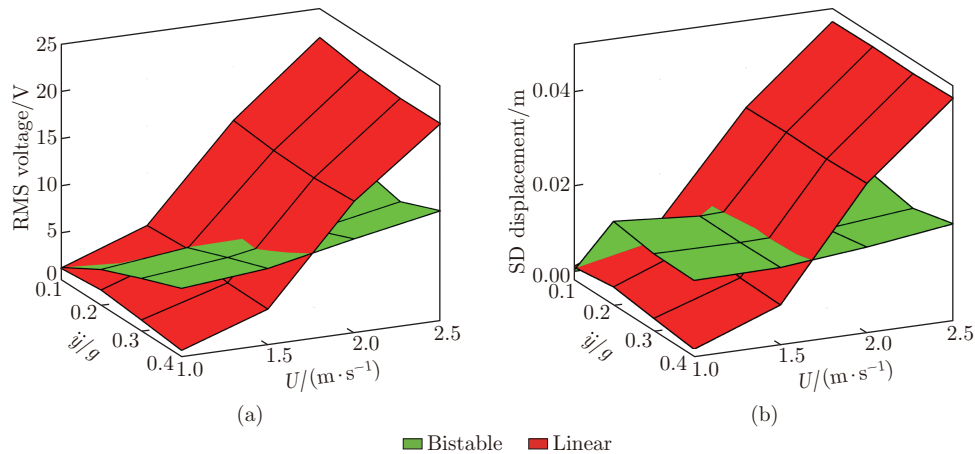

Fig. 10 (a) 3-D diagram of acceleration-wind speed-RMS voltage; (b) 3-D diagram of acceleration-wind speed-SD displacement (color online)

superior performance compared with the LEH. However, as the wind speed is increased to realize galloping, the dynamic response of the LEH is more pronounced than that of the bistable counterpart.

Figures 11 and 12 show a comparison between the BEH-GR and the LEH-GR in terms of the time domain response of displacements and voltages, respectively. If the energy harvester is under the influence of two wind speeds of $U = 1\,\mathrm{m/s}$ and $U = 1.5\,\mathrm{m/s}$, the transient displace-
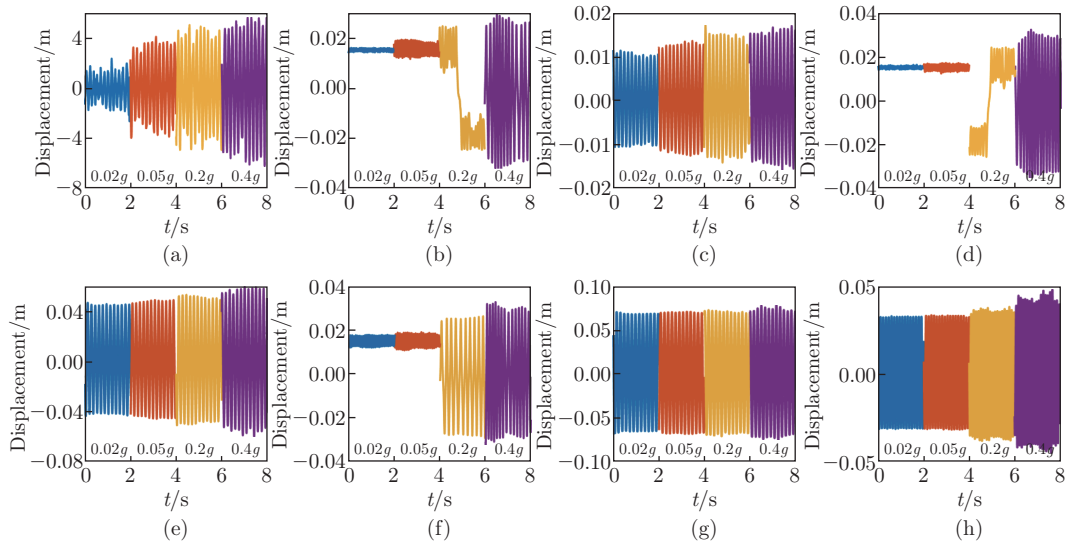

Fig. 11 Experimental time-domain displacement responses of LEH-GR and BEH-GR. (a) and (b): $U = 1\,\mathrm{m/s}$; (c) and (d): $U = 1.5\,\mathrm{m/s}$; (e) and (f): $U = 2\,\mathrm{m/s}$; (g) and (h): $U = 2.5\,\mathrm{m/s}$. The lines of blue, brown, yellow, and purple represent the time domain displacement responses under the random excitation levels of $0.02g$, $0.05g$, $0.2g$, and $0.4g$, respectively (color online)
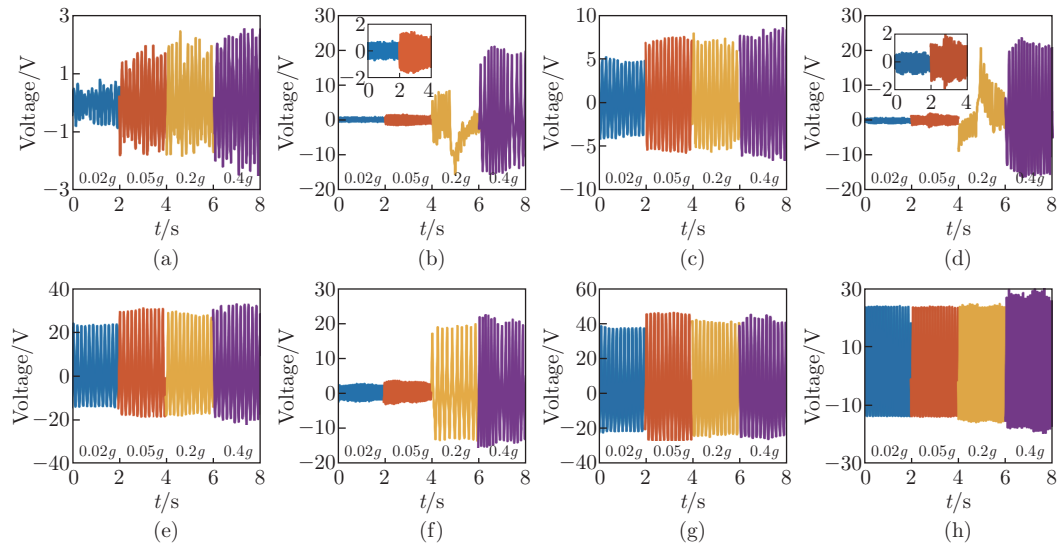

Fig. 12 Experimental time-domain voltage responses of LEH-GR and BEH-GR. (a) and (b): $U = 1\,\mathrm{m/s}$; (c) and (d): $U = 1.5\,\mathrm{m/s}$; (e) and (f): $U = 2\,\mathrm{m/s}$; (g) and (h): $U = 2.5\,\mathrm{m/s}$. The lines of blue, brown, yellow, and purple represent the time domain voltage responses under the random excitation levels of $0.02g$, $0.05g$, $0.2g$, and $0.4g$, respectively (color online)

ment response of the LEH oscillates around the only static equilibrium position for four levels of random accelerations, as shown in Figs. 11(a), 11(c), 12(a), and 12(c). However, the BEH achieves inter-well vibration and an irregular large pulse voltage as the excitation level is $0.2g$ (see Figs. 11(b), 11(d), 12(b), and 12(d)). On the contrary, when the speed of incoming wind exceeds $U = 2\,\mathrm{m/s}$, the LEH generates larger mechanical and electrical responses compared with the BEH.

To quantify the comparative results of experiments and simulations, the RMS voltages obtained from numerical simulations and experiments at four excitation levels are shown in Table 2. Both numerical simulations and experiments demonstrate that the response of BEH-GR is inferior to that of the LEH-GR as the speed of wind is set to $U = 2\,\mathrm{m/s}$. In general, the relative error of BEH is higher than that of LEH due to magnetic induced nonlinearities. Especially for the BEH under a low random base acceleration of $0.02g$, the maximal error between numerical simulations and experiments attains 25%. As the random excitation level increases, the relative error decreases gradually. The primary reason for this phenomenon is that, for a low random excitation level, the response is restricted to oscillate around the single equilibrium, showing large randomness. As the excitation goes up, the energy harnessed by the system also increases. The system escapes from the restriction of a potential well, and weakens the randomness while enhancing the periodicity.

Table 2   Demographic prediction performance comparison by three evaluation metrics

Excitation level	Numerical simulation RMS voltage/V		Experiment verification RMS voltage/V		Error/%	
	LEH-GR	BEH-GR	LEH-GR	BEH-GR	LEH-GR	BEH-GR
$0.02g$	12.3	2.0	12.8	1.6	4	25
$0.05g$	15.6	2.5	16.6	1.9	6	24
$0.2g$	15.7	10.8	15.5	9.2	1.2	14.8
$0.4g$	17.2	11.5	17.6	10.8	2.2	2.2

5   Conclusions

To reveal the intrinsic correlation between band-limited random vibration and incoming wind on energy harvesting performance, this paper provides a comprehensive investigation on the BEH-GR. The SAM-based energy envelope is used to analyze the influence of wind speed and random excitation levels on the dynamic response. The analytical results are verified with the MCM. Experimental verification is conducted to characterize and compare the dynamic response of BEH-GR and its linear counterpart. By analyzing the results of numerical simulations and experiments, the following conclusions are drawn.

With the enhancement in the random excitation level and wind speed, the PDF increases in the regions of non-equilibrium. In particular, as the speed of wind strengthens to a particular level, the influence of the random excitation is weakened, and the JPDF presents an annulus in the phase plane. The scope of the annulus gradually increases with the increasing wind speed.

For the BEH-GR, the threshold of random excitation level for triggering inter-well vibration is significantly reduced. Thus, a combination excitation of galloping and random vibrations is conducted to realize the improvement in the bi-stable energy harvesting performance.

However, both the numerical simulations and experiments find that bi-stable structures are not always beneficial for harvesting hybrid excitation. Under the effects of low-speed wind, strong random excitation is apparently suitable for the BEH in comparison with the LEH. But once the speed of incoming wind is larger than the threshold for galloping, the benefits of bi-stable systems in capturing hybrid excitation disappear regardless of the random excitation level.

References

[1] YANG, Z., ZHOU, S., ZU, J., and INMAN, D. High-performance piezoelectric energy harvesters and their applications. *Joule*, **2**, 642–697 (2018)

[2] CAO, D., WANG, J., GUO, X., LAI, S. K., and SHEN, Y. Recent advancement of flow-induced piezoelectric vibration energy harvesting techniques: principles, structures, and nonlinear designs. *Applied Mathematics and Mechanics* (*English Edition*), **43**(7), 959–978 (2022) https://doi.org/10.1007/s10483-022-2867-7

[3] DAQAQ, M. F., MASANA, R., ERTURK, A., and QUINN, D. D. On the role of nonlinearities in vibratory energy harvesting: a critical review and discussion. *Applied Mechanics Reviews*, **66**, 040801 (2014)

[4] WEI, C. and JING, X. A comprehensive review on vibration energy harvesting: modelling and realization. *Renewable and Sustainable Energy Reviews*, **74**, 1–18 (2017)

[5] WANG, L. and YUAN, F. G. Vibration energy harvesting by magnetostrictive material. *Smart Materials and Structures*, **17**, 1–18 (2008)

[6] HUYNH, B. H., TJAHJOWIDODO, T., ZHONG, Z. W., WANG, Y., and SRIKANTH, N. Design and experiment of controlled bistable vortex induced vibration energy harvesting systems operating in chaotic regions. *Mechanical Systems and Signal Processing*, **98**, 1097–1115 (2018)

[7] FU, Y., OUYANG, H., and BENJAMIN, D. R. Nonlinear structural dynamics of a new sliding-mode triboelectric energy harvester with multistability. *Nonlinear Dynamics*, **100**, 1941–1962 (2020)

[8] QIAN, F., ZHOU, S., and ZUO, L. Approximate solutions and their stability of a broadband piezoelectric energy harvester with a tunable potential function. *Communications in Nonlinear Science and Numerical Simulation*, **80**, 104984 (2020)

[9] LI, H. T., DING, H., JING, X. J., QIN, W. Y., and CHEN, L. Q. Improving the performance of a tri-stable energy harvester with a staircase-shaped potential well. *Mechanical Systems and Signal Processing*, **25**, 107805 (2021)

[10] LAI, S. K., WANG, C., and ZHANG, L. H. A nonlinear multi-stable piezomagnetoelastic harvester array for low-intensity, low-frequency, and broadband vibrations. *Mechanical Systems and Signal Processing*, **122**, 87–102 (2019)

[11] DENG, T. C. and DING, H. Frequency band preservation: pipe design strategy away from resonance. *Acta Mechanica Sinica*, **40**(3), 523201 (2024)

[12] CHEN, H. Y., MAO, X. Y., DING, H., and CHEN, L. Q. Elimination of multimode resonances of composite plate by inertial nonlinear energy sinks. *Mechanical Systems and Signal Processing*, **135**, 106383 (2020)

[13] CHEN, L. Q. and JIANG, W. A. Internal resonance energy harvesting. *Journal of Applied Mechanics*, **82**, 031004 (2015)

[14] YUAN, T., YANG, J., and CHEN, L. Q. Nonlinear characteristic of a circular composite plate energy harvester: experiments and simulations. *Nonlinear Dynamics*, **90**, 2495–2506 (2017)

[15] YUAN, T., YANG, J., and CHEN, L. Q. Nonlinear dynamics of a circular piezoelectric plate for vibratory energy harvesting. *Communications in Nonlinear Science and Numerical Simulation*, **59**, 651–666 (2018)

[16] ZHOU, W., WANG, B., LIM, C. W., and YANG, Z. A distributed-parameter electromechanical coupling model for a segmented arc-shaped piezoelectric energy harvester. *Mechanical Systems and Signal Processing*, **146**, 107005 (2020)

[17] FAN, K., CAI, M., LIU, H., and ZHANG, Y. Capturing energy from ultra-low frequency vibrations and human motion through a monostable electromagnetic energy harvester. *Energy*, **169**, 356–368 (2019)

[18] WANG, C., ZHANG, Q., and WANG, W. Low-frequency wideband vibration energy harvesting by using frequency up-conversion and quin-stable nonlinearity. *Journal of Sound and Vibration*, **399**, 169–181 (2017)

[19] VOCCA, H., NERI, I., TRAVASSO, F., and GAMMAITONI, L. Kinetic energy harvesting with bistable oscillators. *Applied Energy*, **97**, 771–776 (2012)

[20] LU, Z., LI, K., DING, H., and CHEN, L. Nonlinear energy harvesting based on a modified snap-through mechanism. *Applied Mathematics and Mechanics* (*English Edition*), **40**(1), 167–180 (2019) https://doi.org/10.1007/s10483-019-2408-9

[21] LI, H. T., QIN, W. Y., ZU, J., and YANG, Z. Modeling and experimental validation of a buckled compressive-mode piezoelectric energy harvester. *Nonlinear Dynamics*, **92**, 1761–1780 (2018)

[22] ZHAO, L. C., ZOU, H. X., YAN, G., ZHANG, W. M., PENG, Z. K., and MENG, G. Arbitrary-directional broadband vibration energy harvesting using magnetically coupled flextensional transducers. *Smart Materials and Structures*, **27**, 095010 (2018)

[23] YANG, W. and TOWFIGHIAN, S. A hybrid nonlinear vibration energy harvester. *Mechanical Systems and Signal Processing*, **90**, 317–333 (2017)

[24] LALLART, M., ZHOU, S., YAN, L., YANG, Z., and CHEN, Y. Tailoring multistable vibrational energy harvesters for enhanced performance: theory and numerical investigation. *Nonlinear Dynamics*, **96**, 1283–1301 (2019)

[25] YANG, T., CAO, Q., LI, Q., and QIU, H. A multi-directional multi-stable device: modeling, experiment verification and applications. *Mechanical Systems and Signal Processing*, **146**, 106986 (2020)

[26] ZHANG, J., YANG, K., and LI, R. A bistable nonlinear electromagnetic actuator with elastic boundary for actuation performance improvement. *Nonlinear Dynamics*, **100**, 3575–3596 (2020)

[27] STANTON, S. C., MCGEHEE, C. C., and MANN, B. P. Nonlinear dynamics for broadband energy harvesting: investigation of a bistable piezoelectric inertial generator. *Physica D*: *Nonlinear Phenomena*, **239**, 640–653 (2010)

[28] ERTURK, A., HOFFMANN, J., and INMAN, D. J. A piezomagnetoelastic structure for broadband vibration energy harvesting. *Applied Physics Letters*, **94**, 254102 (2009)

[29] CAO, J., WANG, W., ZHOU, S., INMAN, D. J., and LIN, J. Nonlinear time-varying potential bistable energy harvesting from human motion. *Applied Physics Letters*, **107**, 143904 (2015)

[30] ZHOU, Z., QIN, W., DU, W., ZHU, P., and LIU, Q. Improving energy harvesting from random excitation by nonlinear flexible bi-stable energy harvester with a variable potential energy function. *Mechanical Systems and Signal Processing*, **115**, 162–172 (2019)

[31] HAO, M. Y., DING, H., MAO, X. Y., and CHEN, L. Q. Multi-harmonic resonance of pipes conveying fluid with pulsating flow. *Journal of Sound and Vibration*, **569**, 117990 (2024)

[32] COTTONE, F., GAMMAITONI, L., VOCCA, H., FERRARI, M., and FERRARI, V. Piezoelectric buckled beams for random vibration energy harvesting. *Smart Materials and Structures*, **21**, 035021 (2012)

[33] ZHAO, S. and ERTURK, A. Electroelastic modeling and experimental validations of piezoelectric energy harvesting from broadband random vibrations of cantilevered bimorphs. *Smart Materials and Structures*, **2**, 015002 (2013)

[34] FANG, S., FU, X., and LIAO, W. H. Asymmetric plucking bistable energy harvester: modeling and experimental validation. *Journal of Sound and Vibration*, **459**, 114852 (2019)

[35] XU, M., WANG, B., LI, X., ZHOU, S., and YURCHENKO, D. Dynamic response mechanism of the galloping energy harvester under fluctuating wind conditions. *Mechanical Systems and Signal Processing*, **166**, 108410 (2022)

[36] JIANG, W. A., SUN, P., ZHAO, G. L., and CHEN, L. Q. Path integral solution of vibratory energy harvesting systems. *Applied Mathematics and Mechanics* (*English Edition*), **40**(4), 579-590 (2019) https://doi.org/10.1007/s10483-019-2467-8

[37] BARRERO-GIL, A., ALONSO, G., and SANZ-ANDRES, A. Energy harvesting from transverse galloping. *Journal of Sound and Vibration*, **329**, 2873-2883 (2010)

[38] ABDELKEFI, A., YAN, Z., and HAJJ, M. R. Modeling and nonlinear analysis of piezoelectric energy harvesting from transverse galloping. *Smart Materials and Structures*, **22**, 025016 (2013)

[39] LI, H., DING, H., and CHEN, L. Chaos threshold of a multistable piezoelectric energy harvester subjected to wake-galloping. *International Journal of Bifurcation and Chaos*, **29**, 1950162 (2019)

[40] TAN, T., HU, X., YAN, Z., and ZHANG, W. Enhanced low-velocity wind energy harvesting from transverse galloping with super capacitor. *Energy*, **187**, 115915 (2019)

[41] WANG, J., ZHAO, W., SU, Z., ZHANG, G., LI, P., and YURCHENKO, D. Enhancing vortex-induced vibrations of a cylinder with rod attachments for hydrokinetic power generation. *Mechanical Systems and Signal Processing*, **145**, 106912 (2020)

[42] TANG, L., ZHAO, L., YANG, Y., and LEFEUVRE, E. Equivalent circuit representation and analysis of galloping-based wind energy harvesting. *IEEE-ASME Transactions on Mechatronics*, **20**, 834–844 (2015)

[43] JAVED, U. and ABDELKEFI, A. Impacts of the aerodynamic force representation on the stability and performance of a galloping-based energy harvester. *Journal of Sound and Vibration*, **400**, 213–226 (2017)

[44] DAI, H. L., ABDELKEFI, A., JAVED, U., and WANG, L. Modeling and performance of electromagnetic energy harvesting from galloping oscillations. *Smart Materials and Structures*, **24**, 045012 (2015)

[45] DAI, H. L., YANG, Y. W., ABDELKEFI, A., and WANG, L. Nonlinear analysis and characteristics of inductive galloping energy harvesters. *Communications in Nonlinear Science and Numerical Simulation*, **59**, 580–591 (2018)

[46] ZHOU, Z., QIN, W., ZHU, P., and SHANG, S. Scavenging wind energy by a Y-shaped bi-stable energy harvester with curved wings. *Energy*, **153**, 400–412 (2018)

[47] ABDELMOULA, H. and ABDELKEFI, A. Investigations on the presence of electrical frequency on the characteristics of energy harvesters under base and galloping excitations. *Nonlinear Dynamics*, **89**, 2461–2479 (2017)

[48] BIBO, A., ABDELKEFI, A., and DAQAQ, M. F. Modeling and characterization of a piezoelectric energy harvester under combined aerodynamic and base excitations. *Journal of Vibration and Acoustics*, **137**, 031017 (2015)

[49] BIBO, A. and DAQAQ, M. F. Energy harvesting under combined aerodynamic and base excitations. *Journal of Sound and Vibration*, **332**, 5086–5102 (2013)

[50] LIU, H. and GAO, X. Vibration energy harvesting under concurrent base and flow excitations with internal resonance. *Nonlinear Dynamics*, **96**, 1067–1081 (2019)

[51] YAN, Z. and ABDELKEFI, A. Nonlinear characterization of concurrent energy harvesting from galloping and base excitations. *Nonlinear Dynamics*, **77**, 1171–1189 (2014)

[52] ZHAO, L. and YANG, Y. An impact-based broadband aeroelastic energy harvester for concurrent wind and base vibration energy harvesting. *Applied Energy*, **212**, 233–243 (2018)

[53] LI, H. T., DONG, B. J., CAO, F., QIN, W. Y., DING, H., and CHEN, L. Q. Nonlinear dynamical and harvesting characteristics of bistable energy harvester under hybrid base vibration and galloping. *Communications in Nonlinear Science and Numerical Simulation*, **125**, 107400 (2023)

[54] YANG, K., ABDELKEFI, A., LI, X., MAO, Y., DAI, L., and WANG, J. Stochastic analysis of a galloping-random wind energy harvesting performance on a buoy platform. *Energy Conversion and Management*, **238**, 114174 (2021)